

# OGLE-2013-BLG-0102LA,B: MICROLENSING BINARY WITH COMPONENTS AT STAR/BROWN-DWARF AND BROWN-DWARF/PLANET BOUNDARIES

Y. K. JUNG<sup>1</sup>, A. UDALSKI<sup>01,O</sup>, T. SUMI<sup>M1,M</sup>, C. HAN<sup>1,U,†</sup>, A. GOULD<sup>U1,U</sup>,  
AND

J. SKOWRON<sup>01</sup>, S. KOZŁOWSKI<sup>01</sup>, R. POLESKI<sup>01,U1</sup>, Ł. WYRZYKOWSKI<sup>01,02</sup>, M. K. SZYMAŃSKI<sup>01</sup>, G. PIETRZYŃSKI<sup>01,03</sup>,  
I. SOSZYŃSKI<sup>01</sup>, K. ULACZYK<sup>01</sup>, P. PIETRUKOWICZ<sup>01</sup>, P. MRÓZ<sup>01</sup>, M. KUBIAK<sup>01</sup>

(THE OGLE COLLABORATION),

F. ABE<sup>M2</sup>, D. P. BENNETT<sup>M3</sup>, I. A. BOND<sup>M4</sup>, C. S. BOTZLER<sup>M5</sup>, M. FREEMAN<sup>M5</sup>, A. FUKUI<sup>M6</sup>, D. FUKUNAGA<sup>M2</sup>, Y. ITOW<sup>M2</sup>,  
N. KOSHIMOTO<sup>M1</sup>, P. LARSEN<sup>M7</sup>, C. H. LING<sup>M4</sup>, K. MASUDA<sup>M2</sup>, Y. MATSUBARA<sup>M2</sup>, Y. MURAKI<sup>M2</sup>, S. NAMBA<sup>M1</sup>, K. OHNISHI<sup>M8</sup>,  
L. PHILPOTT<sup>M9</sup>, N. J. RATTENBURY<sup>M5</sup>, TO. SAITO<sup>M10</sup>, D. J. SULLIVAN<sup>M11</sup>, D. SUZUKI<sup>M1</sup>, P. J. TRISTRAM<sup>M12</sup>, N. TSURUMI<sup>M2</sup>,  
K. WADA<sup>M1</sup>, N. YAMAI<sup>M13</sup>, P. C. M. YOCK<sup>M5</sup>, A. YONEHARA<sup>M13</sup>

(THE MOA COLLABORATION),

M. ALBROW<sup>U2</sup>, J.-Y. CHOI<sup>1</sup>, D. L. DEPOY<sup>U3</sup>, B. S. GAUDI<sup>U1</sup>, K.-H. HWANG<sup>1</sup>, C.-U. LEE<sup>U4</sup>, H. PARK<sup>1</sup>, S. OWEN<sup>U1</sup>, R. W. POGGE<sup>U1</sup>,  
I.-G. SHIN<sup>1</sup>, J. C. YEE<sup>U1,U5</sup>

(THE  $\mu$ FUN COLLABORATION)

<sup>1</sup>Department of Physics, Chungbuk National University, Cheongju 371-763, Republic of Korea

<sup>01</sup>Warsaw University Observatory, Al. Ujazdowskie 4, 00-478 Warszawa, Poland

<sup>02</sup>Institute of Astronomy, University of Cambridge, Madingley Road, Cambridge CB3 0HA, UK

<sup>03</sup>Universidad de Concepción, Departamento de Astronomía, Casilla 160-C, Concepción, Chile

<sup>M1</sup>Department of Earth and Space Science, Osaka University, Osaka 560-0043, Japan

<sup>M2</sup>Solar-Terrestrial Environment Laboratory, Nagoya University, Nagoya, 464-8601, Japan

<sup>M3</sup>Department of Physics, University of Notre Dame, 225 Nieuwland Science Hall, Notre Dame, IN 46556-5670, USA

<sup>M4</sup>Institute of Information and Mathematical Sciences, Massey University, Private Bag 102-904, North Shore Mail Centre, Auckland, New Zealand

<sup>M5</sup>Department of Physics, University of Auckland, Private Bag 92-019, Auckland 1001, New Zealand

<sup>M6</sup>Okayama Astrophysical Observatory, National Astronomical Observatory of Japan, Asakuchi, Okayama 719-0232, Japan

<sup>M7</sup>Institute of Astronomy, University of Cambridge, Madingley Road, Cambridge CB3 0HA, UK

<sup>M8</sup>Nagano National College of Technology, Nagano 381-8550, Japan

<sup>M9</sup>Department of Physics and Astronomy, The University of British Columbia, 6224 Agricultural Road Vancouver, BC V6T 1Z1, Canada

<sup>M10</sup>Tokyo Metropolitan College of Aeronautics, Tokyo 116-8523, Japan

<sup>M11</sup>School of Chemical and Physical Sciences, Victoria University, Wellington, New Zealand

<sup>M12</sup>Mt. John University Observatory, P.O. Box 56, Lake Tekapo 8770, New Zealand

<sup>M13</sup>Department of Physics, Faculty of Science, Kyoto Sangyo University, 603-8555, Kyoto, Japan

<sup>U1</sup>Department of Astronomy, Ohio State University, 140 West 18th Avenue, Columbus, OH 43210, USA

<sup>U2</sup>Department of Physics and Astronomy, University of Canterbury, Private Bag 4800, Christchurch, New Zealand

<sup>U3</sup>Department of Physics and Astronomy, Texas A&M University, College Station, Texas 77843-4242, USA

<sup>U4</sup>Korea Astronomy and Space Science Institute, 776 Daedukdae-ro, Daejeon, Korea

<sup>U5</sup>Harvard-Smithsonian Center for Astrophysics, 60 Garden St., Cambridge, MA 02138, USA

<sup>O</sup>Optical Gravitational Lensing Experiment (OGLE) Collaboration

<sup>M</sup>Microensing Observations in Astrophysics (MOA) Collaboration

<sup>U</sup>Microensing Follow Up Network ( $\mu$ FUN) Collaboration and

<sup>†</sup>Corresponding author

*Draft version July 12, 2018*

## ABSTRACT

We present the analysis of the gravitational microlensing event OGLE-2013-BLG-0102. The light curve of the event is characterized by a strong short-term anomaly superposed on a smoothly varying lensing curve with a moderate magnification  $A_{\max} \sim 1.5$ . It is found that the event was produced by a binary lens with a mass ratio between the components of  $q = 0.13$  and the anomaly was caused by the passage of the source trajectory over a caustic located away from the barycenter of the binary. From the analysis of the effects on the light curve due to the finite size of the source and the parallactic motion of the Earth, the physical parameters of the lens system are determined. The measured masses of the lens components are  $M_1 = 0.096 \pm 0.013 M_{\odot}$  and  $M_2 = 0.012 \pm 0.002 M_{\odot}$ , which correspond to near the hydrogen-burning and deuterium-burning mass limits, respectively. The distance to the lens is  $3.04 \pm 0.31$  kpc and the projected separation between the lens components is  $0.80 \pm 0.08$  AU.

*Subject headings:* binaries: general, brown dwarfs – gravitational lensing: micro

## 1. INTRODUCTION

It is generally agreed that stars form through the collapse of gas clouds in interstellar medium while planets form either through coagulation of dust in protostellar disks or gravitational instabilities of the gas disk. By contrast, there

exist diverse mechanisms proposed to explain the formation of objects with masses between stars and planets, i.e. very low-mass stars and brown dwarfs, including dynamical interaction (e.g., Boss 2001; Reipurth & Clarke 2001; Umbreit et al. 2005; Bate 2009), photoionizing radiation (e.g., Hester et al. 1996; Whitworth & Zinnecker 2004), disk insta-

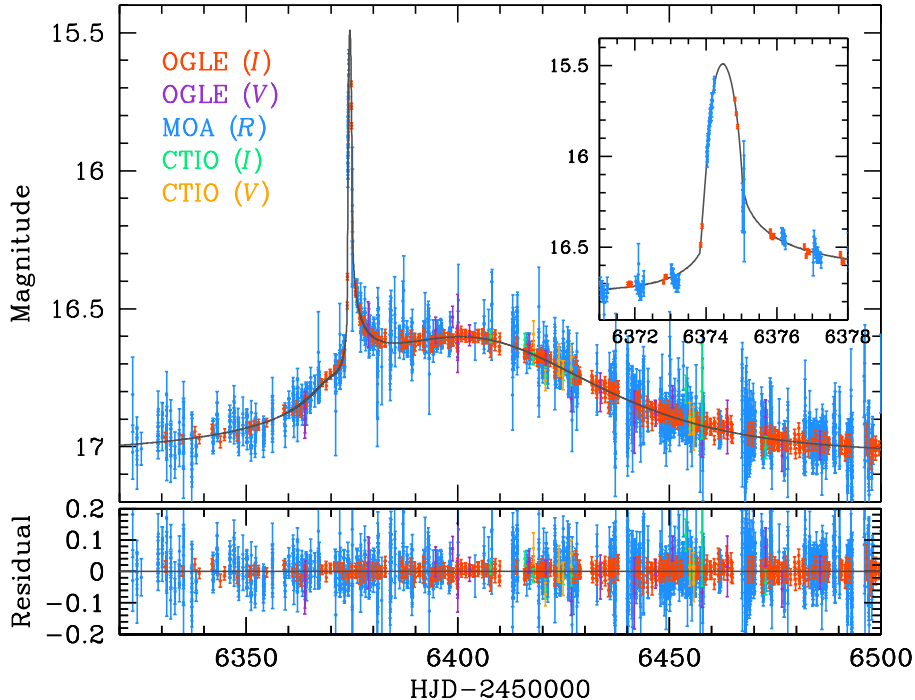


FIG. 1.— Light curve of OGLE-2013-BLG-0102. The inset shows the enlarged view of the anomaly centered at  $\text{HJD}' = \text{HJD} - 2450000 \sim 6374.5$ . The curve superposed on the data is the best-fit model.

bility (e.g., Goodwin & Whitworth 2007; Stamatellos et al. 2007), turbulent fragmentation (e.g., Padoan & Nordlund 2004; Hennebelle & Chabrier 2008), etc. See Luhman (2012) for detailed review.

In order to test formation theories of very low-mass (VLM) objects, various types of observations are needed. In this sense, observational studies of binaries composed of VLM objects are important because predictions of binary properties vary considerably among formation theories. For example, the dynamical interaction and the disk instability mechanisms predict few widely separated binaries while other mechanisms make no concrete predictions on such a trend. Furthermore, with the exception of extreme microlensing events (Gould 1997; Gould et al. 2009) and astrometric microlensing (Cushing et al. 2014) binaries provide the only channel to measure model-independent physical parameters including masses.

Unfortunately, comprehensive studies of VLM binaries have been difficult due to the lack of unbiased samples. Most known low-mass binaries have been discovered by direct imaging (e.g. Close et al. 2003, 2007). Due to the intrinsic nature, faint or dark VLM objects cannot be seen by this method and thus the sample favors binaries with luminous components and roughly equal masses, although some binaries found by other methods such as the “astrometric variable” (e.g. Dahn et al. 2008; Dupuy & Liu 2012; Sahlmann et al. 2013) and “blended light spectroscopy” (e.g. Burgasser et al. 2010; Bardalez Gagliuffi et al. 2014) have little or no such bias. In addition, since it is difficult to detect closely separated ( $\lesssim 1$  AU) binary systems due to the limitation set by angular resolution, the sample is biased toward widely separated binaries. For the same reason, the sample is confined to binaries in the Solar neighborhood. Furthermore, spectroscopic radial-velocity observations for these objects are difficult due to their faintness and thus it is difficult to precisely measure

their masses.

Because of the difference in sensitivity from other methods, gravitational microlensing provides a complementary tool to study VLM objects. Microlensing occurs due to the bending of light caused by the gravity of a lensing object located between an observer and a lensed star (source). As a result, the phenomenon does not depend on the brightness of lensing objects, making it possible to detect faint and even dark objects. Lensing events occur in Galactic scale and thus the method can be used to detect VLM binaries distributed over a wide range of Galactocentric distances. In addition, the method is sensitive to tight binaries with small separations (Choi et al. 2013). Furthermore, for well observed binary-lens events, it is possible to precisely measure binary masses without additional follow-up observations. The method already demonstrated the usefulness in detecting VLM objects existing in various forms, e.g. a free-floating brown dwarf (Gould et al. 2009), binary brown dwarfs (Choi et al. 2013), brown dwarfs around stars (Shin et al. 2012; Street et al. 2013), and a brown dwarf orbited by a planetary mass object (Han et al. 2013).

In this paper, we report a low-mass binary discovered from the observation of the microlensing event OGLE-2013-BLG-0102. We demonstrate that the binary is composed of a primary near the hydrogen-burning limit and a companion near the deuterium-burning limit.

## 2. OBSERVATION

The lensing event OGLE-2013-BLG-0102 occurred on a star located toward the Galactic bulge direction with the equatorial coordinates  $(\alpha, \delta)_{J2000} = (17^{\text{h}}52^{\text{m}}07^{\text{s}}.08, -31^{\circ}41'26''.1)$ , corresponding to the Galactic coordinates  $(l, b) = (358.36^{\circ}, -2.626^{\circ})$ . The event was first discovered by the Optical Gravitational Lensing Experiment (OGLE: Udalski 2003) collaboration from the survey conducted toward the Galactic bulge field using the 1.3m Warsaw telescope at Las Campanas Observatory in Chile and the

discovery was announced to the microlensing community on March 2, 2013. The event was independently discovered by the Microlensing Observations in Astrophysics (MOA: Bond et al. 2001; Sumi et al. 2003) collaboration using the 1.8m telescope at Mt. John Observatory in New Zealand and dubbed as MOA-2013-BLG-127. The MOA group noticed that the event had undergone an anomaly and issued a further alert for follow-up observations. No immediate follow-up observation could be done because the anomaly occurred during the very early Bulge season when the duration of the bulge visibility was short and telescopes for follow-up observations were not fully operational. Fortunately, the cadence of the survey observations was high enough to delineate the anomaly covering both the rising and falling parts of the anomaly.

From modeling of the light curve conducted by the time that the anomaly ended, it was suggested that the anomaly was produced by the crossing of a caustic<sup>1</sup> formed by a binary lens where the mass ratio between the components is low. In response to the potential importance of the event, the Microlensing Follow-Up Network ( $\mu$ FUN: Gould et al. 2006) collaboration took multiband images (14 images in *I* band and 12 images in *V* band) during April 25 – June 29 period using the 1.3m SMARTS telescope of Cerro Tololo Inter-American Observatory (CTIO) in Chile to obtain the color information of the source star. The event lasted more than 100 days after the anomaly. From multiple stage real-time modeling of the light curve conducted with the progress of the event, it was suggested that higher-order effects would be needed to precisely describe the event.

Figure 1 shows the light curve of the event. It is characterized by a strong short-term anomaly centered at  $\text{HJD}' = \text{HJD} - 2450000 \sim 6374.5$  superposed on a smooth brightness variation of the source star. The event lasted throughout the whole Bulge season and the anomaly lasted  $\sim 4$  days.

Data sets used for analysis were reduced using photometry codes developed by the individual groups, which are based on difference image analysis (Alard & Lupton 1998). For the use of data sets processed by different photometry systems, we readjust error bars. In this process, we first add a quadratic term so that the cumulative distribution of  $\chi^2$  sorted by magnification becomes approximately linear. We then rescale the error bars so that  $\chi^2$  per degree of freedom ( $\chi^2/\text{dof}$ ) for each data set becomes unity (Dong et al. 2007). The first process is needed to ensure that the dispersion of data points is consistent with error bars regardless of the source brightness. The second process is required to ensure that each data set is fairly weighted according to error bars. We eliminate  $3\sigma$  outliers in the analysis in order to minimize their effect on modeling.

### 3. ANALYSIS

Under the approximation that the relative lens-source motion is rectilinear, the light curve of a binary-lens event is described by 7 standard parameters. See Appendix A for graphical presentation of the parameters. In our modeling of the light curve, we use the center of mass of the binary lens as the reference position.

Searching for the set of lensing parameters that best describes the observed light curve is done through multiple stages. At the first stage, we explore  $\chi^2$  surface in the parameter space and locate all possible local minima by con-

<sup>1</sup> The caustic represents the closed curve of formally infinite magnification on the source plane.

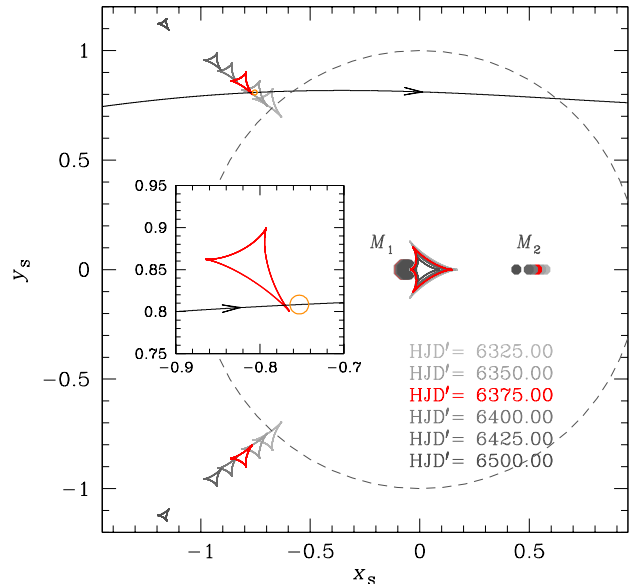


FIG. 2.— Geometry of the source trajectory (curve with an arrow) with respect to the lens components ( $M_1$  and  $M_2$ ) and caustics (closed figures composed of concave curves). The dashed circle represents the Einstein ring. The coordinates are centered at the barycenter of the binary lens and all lengths are scaled to the Einstein radius corresponding to the total mass of the binary. Caustics vary in time due to the lens orbital motion. The red caustics correspond to the time of the anomaly. The inset shows the enlarged view of the source star's caustic crossing. The empty orange circle represents the source size relative to the caustic.

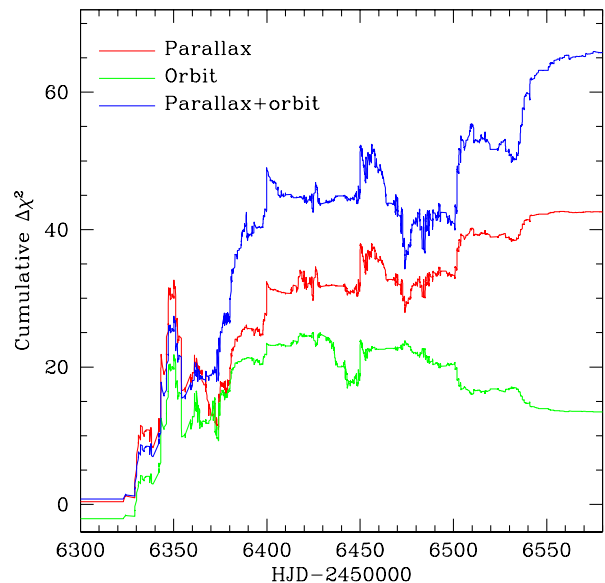


FIG. 3.— Cumulative distributions of  $\Delta\chi^2$  between the models considering higher-order effects relative to the standard model as a function of time.

ducting a grid search for a subset of the lensing parameters. At the second stage, we further refine each local minimum. At the last stage, we identify the global minimum by comparing  $\chi^2$  values of the individual local solutions. Grid search at the first stage is done in the parameter space of  $(s, q, \alpha)$  for which the lensing magnifications can vary dramatically with small changes of the parameters. For the other parameters, for which lensing magnifications vary smoothly for the changes of the parameters, we search for solutions by minimizing  $\chi^2$  using a Markov Chain Monte Carlo (MCMC). Once a solu-

TABLE 1  
 LENSING PARAMETERS

Parameters	Standard	Parallax		Orbit		Orbit+Parallax	
		$u_0 > 0$	$u_0 < 0$	$u_0 > 0$	$u_0 < 0$	$u_0 > 0$	$u_0 < 0$
$\chi^2/\text{dof}$	13472.0/13396	13428.8/13394	13433.9/13394	13459.8/13394	13458.6/13394	13405.0/13392	13422.0/13392
$t_0$ (HJD')	$6406.71 \pm 0.17$	$6406.47 \pm 0.19$	$6406.38 \pm 0.16$	$6405.54 \pm 0.18$	$6405.51 \pm 0.18$	$6406.18 \pm 0.20$	$6406.30 \pm 0.17$
$u_0$	$0.809 \pm 0.010$	$0.832 \pm 0.011$	$-0.827 \pm 0.006$	$0.871 \pm 0.008$	$-0.875 \pm 0.009$	$0.811 \pm 0.011$	$-0.812 \pm 0.008$
$t_E$ (days)	$38.5 \pm 0.3$	$38.9 \pm 0.4$	$39.3 \pm 0.3$	$38.3 \pm 0.3$	$38.2 \pm 0.3$	$37.6 \pm 0.4$	$37.1 \pm 0.4$
$s$	$0.594 \pm 0.003$	$0.595 \pm 0.003$	$0.596 \pm 0.002$	$0.575 \pm 0.002$	$0.573 \pm 0.003$	$0.607 \pm 0.004$	$0.607 \pm 0.002$
$q$	$0.146 \pm 0.005$	$0.112 \pm 0.005$	$0.109 \pm 0.003$	$0.072 \pm 0.002$	$0.067 \pm 0.002$	$0.130 \pm 0.007$	$0.143 \pm 0.002$
$\alpha$ (rad)	$6.36 \pm 0.02$	$6.24 \pm 0.02$	$-6.22 \pm 0.01$	$6.09 \pm 0.01$	$-6.07 \pm 0.01$	$6.36 \pm 0.02$	$-6.39 \pm 0.01$
$\rho_*$ ( $10^{-3}$ )	$10.28 \pm 0.21$	$10.27 \pm 0.30$	$9.91 \pm 0.21$	$8.16 \pm 0.24$	$7.85 \pm 0.16$	$11.12 \pm 0.24$	$11.71 \pm 0.33$
$\pi_{E,N}$	—	$0.11 \pm 0.07$	$-0.01 \pm 0.05$	—	—	$0.48 \pm 0.05$	$-0.44 \pm 0.07$
$\pi_{E,E}$	—	$-0.17 \pm 0.03$	$-0.18 \pm 0.03$	—	—	$-0.06 \pm 0.03$	$-0.20 \pm 0.03$
$ds/dt$ ( $\text{yr}^{-1}$ )	—	—	—	$0.44 \pm 0.05$	$0.51 \pm 0.03$	$-0.31 \pm 0.05$	$-0.48 \pm 0.06$
$d\alpha/dt$ ( $\text{yr}^{-1}$ )	—	—	—	$-1.48 \pm 0.07$	$1.64 \pm 0.04$	$-0.46 \pm 0.18$	$0.05 \pm 0.13$

NOTE. — HJD' = HJD − 2450000

tion is found, the uncertainty of each lensing parameter is estimated based on the distribution of parameters derived from the corresponding MCMC chain.

To model the anomaly, which was produced by the caustic crossing of the source star, it is needed to consider finite-source effects. For the computation of finite magnifications, we use the numerical method of the inverse ray-shooting method (Kayser et al. 1986; Schneider & Weiss 1987) for the central region of the perturbation and semi-analytic hexadecapole approximation (Pejcha & Heyrovský 2009; Gould 2008) for the vicinity of the perturbation. We account for the surface-brightness variation of the source caused by limb darkening by modeling the surface-brightness profile using a linear limb-darkening law. We adopt the limb-darkening coefficients  $(u_V, u_R, u_I) = (0.81, 0.73, 0.63)$  from Claret (2000) using  $T_{\text{eff}} = 4500$  K and  $\log g = 2$ , where  $T_{\text{eff}}$  and  $\log g$  are derived from the de-reddened brightness and color of the source star (see Section 4). For the MOA data taken by using a non-standard filter system, we use  $u_{RI} = (u_R + u_I)/2 = 0.68$ .

For some binary lensing events, the seven basic parameters are not adequate to precisely describe lensing light curves. These cases often occur for long time-scale events where the assumption of the rectilinear lens-source motion is no longer valid. Parallax effects occur due to the change of the observer's position caused by the orbital motion of the Earth around the Sun (Gould 1992; Alcock et al. 1995), causing non-rectilinear source motion. Similarly, lens orbital effects also cause non-rectilinear source motion due to the change of the lens positions caused by the orbital motion of the lens (Dominik 1998; Albrow et al. 2000; Shin et al. 2011; Jung et al. 2013; Park et al. 2013). Parallax effects are described by two parameters  $\pi_{E,N}$  and  $\pi_{E,E}$  which are the two components of the lens parallax vector  $\pi_E$  projected onto the sky along the north and east equatorial coordinates, respectively. The magnitude of  $\pi_E$  corresponds to the ratio of the lens-source relative parallax  $\pi_{\text{rel}}$  to the angular Einstein radius  $\theta_E$ , i.e.

$$\pi_E = \frac{\pi_{\text{rel}}}{\theta_E}; \quad \pi_{\text{rel}} = \text{AU} \left( \frac{1}{D_L} - \frac{1}{D_S} \right), \quad (1)$$

where  $D_L$  and  $D_S$  are the distances to the lens and source, respectively (Gould 2004). The direction of  $\pi_E$  corresponds to the lens-source relative motion. To the first-order approximation, lens-orbital effects are described by two parameters  $ds/dt$  and  $d\alpha/dt$  that represent the change rates of the pro-

jected binary separation and the source-trajectory angle, respectively.

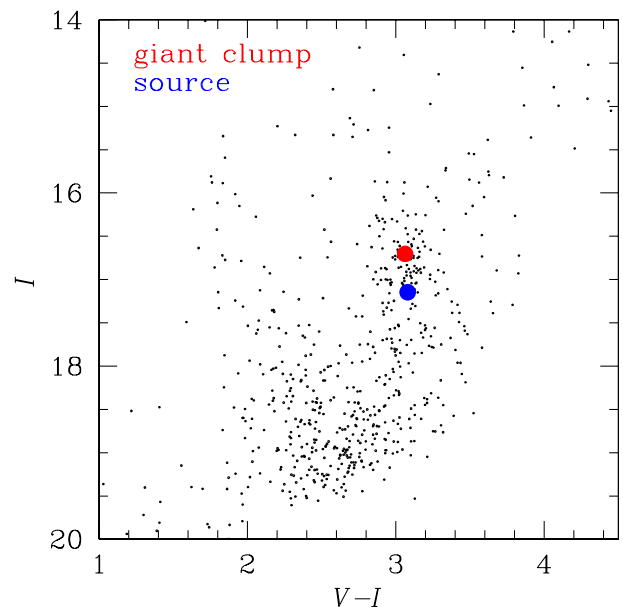


FIG. 4.— Instrumental color-magnitude diagram of stars in the region around the lensed star. The locations of the lensed star (source) and the centroid of giant clump are marked.

Measurements of higher-order effects are important for the determination of the physical lens parameters. By measuring the normalized source radius  $\rho_*$  from the analysis of the light curve affected by finite-source effects, one can measure the Einstein radius by

$$\theta_E = \frac{\theta_*}{\rho_*}, \quad (2)$$

where the angular source radius  $\theta_*$  is derived from the information about the source star (see Section 4). Then, along with the lens parallax measured from the analysis of the long-term deviation caused by parallax effects, the mass and distance to the lens are determined by

$$M_{\text{tot}} = \frac{\theta_E}{\kappa \pi_E}; \quad D_L = \frac{\text{AU}}{\pi_E \theta_E + \pi_S}, \quad (3)$$

respectively. Here  $\kappa = 4G/(c^2 \text{AU})$  and  $\pi_S = \text{AU}/D_S$  is the

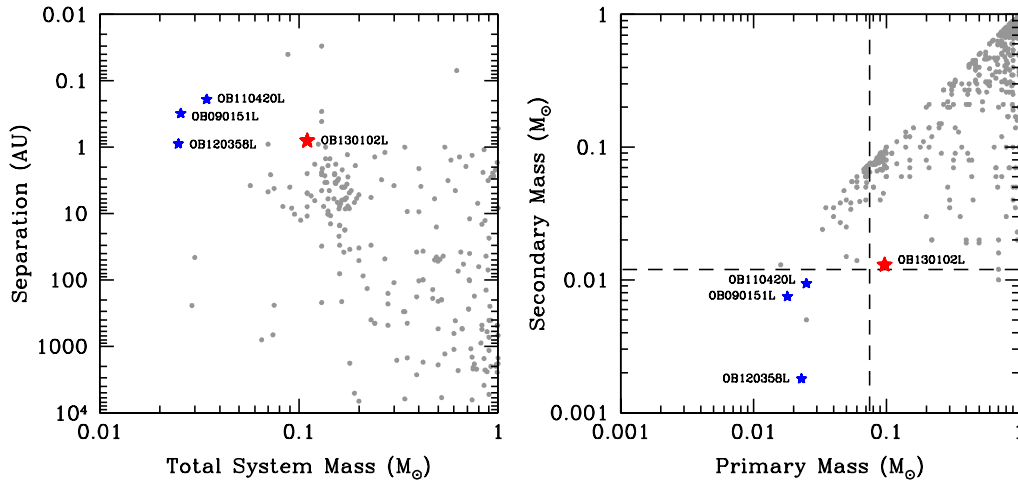


FIG. 5.— Total mass vs. separation (left panel) and primary vs. secondary masses (right panel) for a compilation of low-mass binaries. Microlensing binaries are denoted in ‘star’ marks while those discovered by other methods are marked by dots. The red star is the microlensing binary reported in this work and the three blue stars are the binaries reported by Choi et al. (2013) and Han et al. (2013). The vertical and horizontal dashed lines represent the star/brown-dwarf and brown-dwarf/planet boundaries, respectively.

parallax of the source star.

We test various models considering the individual and combinations of the higher-order effects. In the “standard” model, the light curve is fitted based on the 7 standard lensing parameters. In the “parallax” and “orbit” models, we separately consider the parallax and lens-orbital effects. Finally, in the “orbit+parallax” model, we consider both the parallax and orbital effects. When the higher-order effects are considered, we test two solutions resulting from “ecliptic degeneracy” (Skowron et al. 2011). The two solutions resulting from this degeneracy have almost identical parameters except  $(u_0, \alpha, \pi_{E,N}, d\alpha/dt) \rightarrow -(u_0, \alpha, \pi_{E,N}, d\alpha/dt)$ .

#### 4. PHYSICAL PARAMETERS

In Table 1, we list the results of analysis for the models that we tested. The model light curve of the best-fit solution (orbit+parallax with  $u_0 > 0$ ) is superposed on the data in Figure 1. Figure 2 shows the geometry of the lens system where the source trajectory with respect to the lens positions and caustics are presented. It is found that the event was produced by a binary with a mass ratio between the components is  $q = 0.13$ . The projected separation between the binary components is  $s = 0.61$ , which is less than the Einstein radius. In this case, the caustic is composed of three closed curves where one is located near the barycenter of the binary lens and the other two are located away from the central region. The anomaly was produced by the passage of the source trajectory over one of the outer caustics.

We find that the higher-order effects improve the fit. As measured by  $\chi^2$  difference from the standard model, the fit improvements are  $\Delta\chi^2 = 43.2$  and  $13.4$  when the parallax and orbital effects are separately considered. When both effects are simultaneously considered, the improvement is  $\Delta\chi^2 = 67.0$ , which is  $> 8\sigma$ . While this is formally significant, careful diagnosis of the signal is needed because in microlensing subtle systematic trends might masquerade as signals. We therefore check the possibility of systematics by inspecting where the signal of the higher-order effects comes from. If systematics in data affected the fit, the signal would come from localized epochs of the event. By contrast, if the signal is due to genuine higher-order effects, it would come throughout the event because both the orbital motions of the

TABLE 2  
PHYSICAL PARAMETERS

Parameters	$u_0 > 0$	$u_0 < 0$
Angular Einstein radius (mas)	$0.43 \pm 0.04$	$0.41 \pm 0.03$
Geocentric proper motion (mas yr <sup>-1</sup> )	$4.19 \pm 0.37$	$4.06 \pm 0.34$
Heliocentric proper motion (mas yr <sup>-1</sup> )	$4.30 \pm 0.38$	$3.69 \pm 0.31$
Total mass ( $M_\odot$ )	$0.108 \pm 0.014$	$0.104 \pm 0.017$
Primary mass ( $M_\odot$ )	$0.096 \pm 0.013$	$0.091 \pm 0.015$
Companion mass ( $M_\odot$ )	$0.012 \pm 0.002$	$0.013 \pm 0.002$
Distance (kpc)	$3.04 \pm 0.31$	$3.15 \pm 0.37$
Projected separation (AU)	$0.80 \pm 0.08$	$0.79 \pm 0.09$
(KE/PE) <sub>⊥</sub>	$0.028 \pm 0.006$	$0.037 \pm 0.005$

Earth and the lens have long-term effects on the lensing light curve. In Figure 3, we present the cumulative distribution of  $\Delta\chi^2$  as a function of time. Although there exist several local fluctuations and thus possibility of systematics cannot be completely ruled out,  $\chi^2$  improvement occurs throughout the event, suggesting that the signals of higher-order effects are real. Since the anomaly is well covered, finite-source effects are clearly detected, yielding a normalized source radius  $\rho_* = (11.1 \pm 0.2) \times 10^{-3}$ .

With both finite-source and parallax effects measured, the mass and distance to the lens are estimated by using the relations in Equations (3). For this, we estimate the angular source radius  $\theta_*$  based on the color and brightness. The angular Einstein radius is estimated following two steps. In the first step, we estimate the de-reddened color  $(V-I)_0$  and the brightness  $I_0$  of the source star by using the centroid of Bulge clump giants for which its de-reddened color,  $(V-I)_{0,c} = 1.06$ , and brightness,  $I_{0,c} = 14.45$ , are known from independent measurements (Bensby et al. 2013; Nataf et al. 2013). This method is valid because the source and Bulge giants are at nearly same distances and thus experience almost same extinction (Yoo et al. 2004). The estimated color and brightness of the source star are  $(V-I, I)_0 = (1.08, 14.97)$ . Figure 4 shows the location of the source star in the color-magnitude of neighboring stars with respect to the centroid of clump giants, indicating that the source is a K-type giant. In the second step, we convert  $V-I$  into  $V-K$  by using the color-color relation (Bessell & Brett 1988). Then the angular source

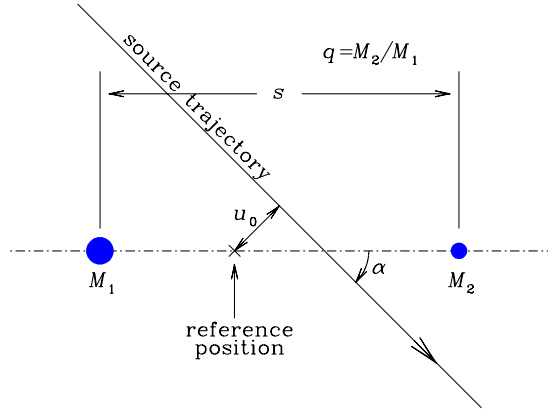


FIG. 6.— Graphical presentation of binary-lensing parameters. The filled dots marked by  $M_1$  and  $M_2$  represent the locations of the lens components. The straight line with an arrow is the source trajectory. The radius is estimated by adopting the relation between  $V-K$  and  $\theta_*$  provided by Kervella et al. (2004). The derived angular source radius is  $\theta_* = 4.80 \pm 0.41 \mu\text{as}$ . The error on  $\theta_*$  comes from three major sources: (1) the uncertainty in the source flux  $f_S$ , (2) the uncertainty involved with the conversion from color to  $\theta_*$ , and (3) other auxiliary uncertainties concerned with processes such as positioning the centroid of giant stars,  $V-I$  to  $V-K$  conversion, etc. We estimate that the uncertainty in  $f_S$  is  $\sigma_{f_S} = 5\%$ . Uncertainties of microlensing colours  $\sigma_{(V-I)_0} = 0.07 \text{ mag}$  (Bensby et al. 2013) and brightness  $\sigma_{I_{0,c}} = 0.09 \text{ mag}$  (Nataf et al. 2013) of clump giant stars contribute  $\sim 6\%$  error in  $\theta_*$  measurement. By considering other factors, we adopt the uncertainty from factors (2) and (3) as 7%. The estimated source radius corresponds to the angular Einstein radius  $\theta_E = 0.43 \pm 0.04 \text{ mas}$ .

In Table 2, we summarize the determined physical quantities of the lens system. We present 2 sets of quantities corresponding to the  $u_0 > 0$  and  $u_0 < 0$  solutions resulting from the ecliptic degeneracy. It is found that the  $u_0 > 0$  model is preferred by  $\Delta\chi^2 = 17.0$ . This is formally  $> 4\sigma$  level, but one cannot completely rule out  $u_0 < 0$  model considering possible systematics in data. However, we note that both solutions result in similar physical quantities. According to the best-fit model, the masses of the lens components are  $M_1 = 0.096 \pm 0.013 M_\odot$  and  $M_2 = 0.012 \pm 0.002 M_\odot$ . The distance to the lens is  $D_L = 3.04 \pm 0.31 \text{ kpc}$  and the projected separation between the lens components is  $r_\perp = s D_L \theta_E = 0.80 \pm 0.08 \text{ AU}$ . In order to check the validity of the solution, we also present the *projected* kinetic to potential energy ratio, which is computed by

$$\left(\frac{\text{KE}}{\text{PE}}\right)_\perp = \frac{(r_\perp/\text{AU})^2}{8\pi^2(M_{\text{tot}}/M_\odot)} \left[ \left(\frac{1}{s} \frac{ds}{dt}\right)^2 + \left(\frac{d\alpha}{dt}\right)^2 \right], \quad (4)$$

where  $M_{\text{tot}}$  is the total mass of the binary-lens (Dong et al. 2009). We note that the lensing parameters  $ds/dt$  and  $d\alpha/dt$  are determined from modeling considering the orbital motion of the lens. The ratio should be less than unity to be a bound system. The measured ratio is  $(\text{KE}/\text{PE})_\perp < 1.0$  and thus meets the condition of boundness. Its small value tends to imply that the true separation is several times larger than the projected separation.

In Figure 5, we compare the physical parameters of OGLE-2013-BLG-0102L to those of low-mass binaries from the VLM binaries archive (<http://www.vlmbinaries.org>) and other references (Basri & Martín 1999; Lane et al. 2001;

Burgasser et al. 2008; Faherty et al. 2011; Burgasser et al. 2012). Also marked are the three low-mass microlensing binaries: OGLE-2009-BLG-151L and OGLE-2011-BLG-420L reported by Choi et al. (2013) and OGLE-2012-BLG-0358L reported by Han et al. (2013). It is found that the microlensing binaries are located in the low-mass, close-separation, and low-mass-ratio regions in the parameter space. Among known VLM binaries, we find that only ‘Cha H $\alpha$  8’ has similar physical parameters:  $r_\perp = 1.3 \text{ AU}$ ,  $M_1 = 0.1 M_\odot$ ,  $M_2 = 0.019 M_\odot$  (Joergens 2006; Joergens & Müller 2007). However, this binary was discovered in a star-forming cloud and thus very young. Therefore, the reported VLM binary demonstrates that microlensing provide an important method that can complement other methods.

The discovered binary is of scientific interest because the masses of the primary and the companion correspond to the upper and lower limits of brown dwarfs, respectively. Although there exist some dispute, the popular convention for the division between low-mass stars and brown dwarfs is  $\sim 0.075 M_\odot$ , below which hydrogen fusion reaction in cores does not occur (Burrows et al. 1997), while the convention for the division between brown dwarfs and giant planets is  $\sim 0.012 M_\odot$  ( $13 M_J$ ), below which deuterium burning cannot be ignited (Spiegel et al. 2011). Then, the individual binary components of OGLE-2013-BLG-0102L have masses near the hydrogen-burning and deuterium-burning mass limits, respectively.

## 5. CONCLUSION

We found a very low-mass binary from the observation and analysis of the microlensing event OGLE-2013-BLG-0102. The event was characterized by a strong short-term anomaly superposed on a smoothly varying lensing curve with a moderate magnification. It was found that the event was produced by a binary object with a mass ratio between the components is  $q = 0.13$  and the anomaly was caused by the passage of the source trajectory over a caustic located away from the barycenter of the binary lens. By measuring deviations in lensing light curve caused by both finite-source and parallax effects, we determined the physical parameters of the lens. It was found that the lens is composed of objects with masses  $M_1 = 0.096 \pm 0.013 M_\odot$  and  $M_2 = 0.012 \pm 0.002 M_\odot$ , which correspond to the hydrogen-burning and deuterium-burning limits, respectively. The binary is located at a distance  $3.04 \pm 0.31 \text{ kpc}$  and the projected separation between the components is  $0.80 \pm 0.08 \text{ AU}$ .

Work by C.H. was supported by Creative Research Initiative Program (2009-0081561) of National Research Foundation of Korea. A.G. and B.S.G. acknowledge support from NSF AST-1103471. B.S.G., A.G., and R.W.P. acknowledge support from NASA grant NNX12AB99G. The OGLE project has received funding from the European Research Council under the European Community’s Seventh Framework Programme (FP7/2007-2013)/ERC grant agreement No. 246678 to A.U. The MOA experiment was supported by grants JSPS22403003 and JSPS23340064. T.S. acknowledges the support JSPS 24253004. T.S. is supported by the grant JSPS23340044. Y.M. acknowledges support from JSPS grants JSPS23540339 and JSPS19340058. Work by J.C.Y. was performed in part under contract with the California Institute of Technology (Caltech) funded by NASA through the Sagan Fellowship Program.

APPENDIX  
BINARY-LENSING PARAMETERS

For the basic description of binary-lens events, 7 lensing parameters are needed. Three of these parameters describe the source-lens approach: the time of the closest source approach to a reference position of the lens,  $t_0$ , the separation between the source and the reference position at  $t_0$ ,  $u_0$  (impact parameter), and the time scale for the source to cross the Einstein radius corresponding to the total mass of the binary lens,  $t_E$  (Einstein time scale). Another three parameters describe the binary lens: the mass ratio,  $q = M_2/M_1$ , the projected separation between the lens components,  $s$ , and the angle between the source trajectory and the binary axis,  $\alpha$  (source trajectory angle). See the graphical presentation of the parameters in Figure 6. We note that parameters  $u_0$  and  $s$  are normalized to the angular Einstein radius  $\theta_E$ . The last parameter is the source radius normalized to the Einstein radius,  $\rho_*$  (normalized source radius).

REFERENCES

- Albrow, M. D., Beaulieu, J.-P., Caldwell, J. A. R., et al. 2000, *ApJ*, 534, 894  
 Alcock, C., Allsman, R. A., Alves, D., et al. 1995, *ApJ*, 454, L125  
 Alard, C., & Lupton, R. H. 1998, *ApJ*, 503, 325  
 Bardalez Gagliuffi, D. C., Burgasser, A. J., Gelino, C. R., et al. 2014, *ApJ*, submitted.  
 Basri, G., & Martín, E. L. 1999, *AJ*, 118, 2460  
 Bate, M. R. 2009, *MNRAS*, 392, 590  
 Bensby, T., Yee, J. C., Feltzing, S., et al. 2013, *A&A*, 549, 147  
 Bessell, M. S., & Brett, J. M. 1988, *PASP*, 100, 1134  
 Bond, I. A., Abe, F., Dodd, R. J., et al. 2001, *MNRAS*, 327, 868  
 Boss, A. P. 2001, *ApJ*, 551, L167  
 Burgasser, A. J., Cruz, K. L., Cushing, M., et al. 2010, *ApJ*, 710, 1142  
 Burgasser, A. J., Liu, M. C., Ireland, M. J., et al. 2008, *ApJ*, 681, 579  
 Burgasser, A. J., Luk, C., Dhital, S., et al. 2012, *ApJ*, 757, 110  
 Burgasser, A. J., Reid, I. N., Siegler, N., et al. 2007, in *Protostars and Planets V*, ed. B. Reipurth, D. Jewitt, & K. Keil (Tucson, AZ: Univ. Arizona Press), 427  
 Burrows, A., Marley, M., Hubbard, W. B., et al. 1997, *ApJ*, 491, 856  
 Choi, J.-Y., Han, C., Udalski, A., et al. 2013, *ApJ*, 768, 129  
 Claret, A. 2000, *A&A*, 363, 1081  
 Close, L. M., Siegler, N., Freed, M., et al. 2003, *ApJ*, 587, 407  
 Close, L. M., Zuckerman, B., Song, I., et al. 2007, *ApJ*, 660, 1492  
 Cushing, M. C., Kirkpatrick, J. D., Gelino, C. R., et al. 2014, *AJ*, 147, 113  
 Dahn, C. C., Harris, H. C., Levine, S. E., et al. 2008, *ApJ*, 686, 548  
 Dominik, M. 1998, *A&A*, 329, 361  
 Dong, S., Udalski, A., Gould, A., et al. 2007, *ApJ*, 664, 862  
 Dong, S., Gould, A., Udalski, A., et al. 2009, *ApJ*, 695, 970  
 Dupuy, T. J., & Liu, M. C. 2012, *ApJS*, 201, 19  
 Faherty, J. K., Burgasser, A. J., Bochanski, J. J., et al. 2011, *A&A*, 141, 71  
 Goodwin, S. P., & Whitworth, A. 2007, *A&A*, 466, 943  
 Gould, A. 1992, *ApJ*, 392, 442  
 Gould, A. 1997, *ApJ*, 480, 188  
 Gould, A. 2004, *ApJ*, 606, 319  
 Gould, A. 2008, *ApJ*, 681, 1593  
 Gould, A., Udalski, A., An, D., et al. 2006, *ApJ*, 644, 37  
 Gould, A., Udalski, A., Monard, B., et al. 2009, *ApJ*, 698, L147  
 Han, C., Jung, Y. K., Udalski, A., et al. 2013, *ApJ*, 778, 38  
 Hennebelle, P., & Chabrier, G. 2008, *ApJ*, 684, 395  
 Hester, J. J., Scowen, P. A., Sankrit, R., et al. 1996, *AJ*, 111, 2349  
 Joergens, V. 2006, *A&A*, 446, 1165  
 Joergens, V., & Müller, A. 2007, *ApJ*, 666, 113  
 Jung, Y. K., Han, C., Gould, A., et al. 2013, *ApJ*, 768, L7  
 Kayser, R., Refsdal, S., & Stabell, R. 1986, *A&A*, 166, 36  
 Kervella, P., Bersier, D., Mourard, D., et al. 2004, *A&A*, 428, 587  
 Lane, B. F., Zapatero Osorio, M. R., Britton, M. C., et al. 2001, *ApJ*, 560, 390  
 Luhman, K. L. 2012, *ARA&A*, 50, 65  
 Nataf, D. M., Gould, A., Fouqué, P., et al. 2013, *ApJ*, 769, 88  
 Padoan, P., & Nordlund, A. 2004, *ApJ*, 617, 559  
 Park, H., Udalski, A., Han, C., et al. 2013, *ApJ*, 778, 134  
 Pejcha, O., & Heyrovský, D. 2009, *ApJ*, 690, 1772  
 Reipurth, B., & Clarke, C. 2001, *AJ*, 122, 432  
 Sahlmann, J., Lazorenko, P. F., Ségransan, D., et al. 2013, *A&A*, 556, 133  
 Schneider, P., & Weiss, A. 1987, *A&A*, 171, 49  
 Shin, I.-G., Han, C., Gould, A., et al. 2012, *ApJ*, 760, 116  
 Shin, I.-G., Udalski, A., Han, C., et al. 2011, *ApJ*, 735, 85  
 Skowron, J., Udalski, A., Gould, A., et al. 2011, *ApJ*, 738, 87  
 Spiegel, D. S., Burrows, A., & Milsom, J. A. 2011, *ApJ*, 727, 57  
 Stamatellos, D., Hubber, D. A., & Whitworth, A. P. 2007, *MNRAS*, 382, L30  
 Street, R., Choi, J.-Y., Tsapras, Y., et al. 2013, *ApJ*, 763, 67  
 Sumi, T., Abe, F., Bond, I. A., et al. 2003, *ApJ*, 591, 204  
 Udalski, A. 2003, *Acta Astron.*, 53, 291  
 Umbreit, S., Burkert, A., Henning, T., et al. 2005, *ApJ*, 623, 940  
 Whitworth, A. P., & Zinnecker, H. 2004, *A&A*, 427, 299  
 Yoo, J., DePoy, D. L., Gal-Yam, A., et al. 2004, *ApJ*, 603, 139